Diffraction phase microscopy: monitoring nanoscale dynamics in materials science [Invited]

Chris Edwards,[1,2] Renjie Zhou,[1,2] Suk-Won Hwang,[3] Steven J. McKeown,[1] Kaiyuan Wang,[1] Basanta Bhaduri,[2] Raman Ganti,[4] Peter J. Yunker,[4,5] Arjun G. Yodh,[4] John A. Rogers,[3] Lynford L. Goddard,[1] and Gabriel Popescu[2,*]

[1]Photonic Systems Laboratory, Micro and Nanotechnology Laboratory, Department of Electrical and Computer Engineering, University of Illinois at Urbana-Champaign, Urbana, Illinois 61801, USA

[2]Quantitative Light Imaging Laboratory, Department of Electrical and Computer Engineering, Beckman Institute for Advanced Science and Technology, University of Illinois at Urbana-Champaign, Urbana, Illinois 61801, USA

[3]Rogers Research Group, Department of Materials Science and Engineering, Frederick Seitz Materials Research Laboratory, University of Illinois at Urbana-Champaign, Urbana, Illinois 61801, USA

[4]Department of Physics and Astronomy, University of Pennsylvania, Philadelphia, Pennsylvania 19104, USA

[5]School of Engineering and Applied Sciences, Harvard University, Cambridge, Massachusetts 02138, USA

*Corresponding author: gpopescu@illinois.edu

Received 24 April 2014; revised 17 June 2014; accepted 18 June 2014; posted 20 June 2014 (Doc. ID 210738); published 28 July 2014

Quantitative phase imaging (QPI) utilizes the fact that the phase of an imaging field is much more sensitive than its amplitude. As fields from the source interact with the specimen, local variations in the phase front are produced, which provide structural information about the sample and can be used to reconstruct its topography with nanometer accuracy. QPI techniques do not require staining or coating of the specimen and are therefore nondestructive. Diffraction phase microscopy (DPM) combines many of the best attributes of current QPI methods; its compact configuration uses a common-path off-axis geometry which realizes the benefits of both low noise and single-shot imaging. This unique collection of features enables the DPM system to monitor, at the nanoscale, a wide variety of phenomena in their natural environments. Over the past decade, QPI techniques have become ubiquitous in biological studies and a recent effort has been made to extend QPI to materials science applications. We briefly review several recent studies which include real-time monitoring of wet etching, photochemical etching, surface wetting and evaporation, dissolution of biodegradable electronic materials, and the expansion and deformation of thin-films. We also discuss recent advances in semiconductor wafer defect detection using QPI.

OCIS codes: (170.0110) Imaging systems; (120.3180) Interferometry; (120.4630) Optical inspection; (120.5050) Phase measurement; (160.0160) Materials.

http://dx.doi.org/10.1364/AO.53.000G33

1. Introduction

A. Early Microscopy

In the late 17th century, Antoni van Leeuwenhoek (1632–1723), a Dutch cloth merchant with a passion for grinding and forming his own lenses (which were used to quantify thread counts at the time), handcrafted his own personal high-magnification microscopes and was the first person to discover a previously unknown realm of existence teeming with microscopic life. In a time rife with pseudoscientific speculation, his profound scientific discoveries allowed him to publish hundreds of letters which helped to jump-start the modern field of microscopy [1].

1559-128X/14/270G33-11$15.00/0

Early development in the field of microscopy was hindered by two major bottlenecks: lack of contrast and diffraction-limited resolution. Since most of early microscopy focused on biological specimens, which are typically thin and optically transparent, a lack of contrast was the driving force in the development of new techniques. However, a lack of understanding regarding the underlying theory stymied early development. In 1873, Abbe developed the first useful theory of image formation as the interference of unscattered and scattered light and also calculated the hard limit on image resolution [2]. The development of this theory allowed Zernike to develop the phase contrast technique in 1936 which introduces a phase shift between the scattered and unscattered components, causing the phase information to be mapped into the amplitude [3]. Most detectors, including the human eye, only respond to intensity, so this was the first time that phase information could be observed in microscopy. Other contrast enhancement techniques such as differential interference contrast (DIC or Nomarski) were also developed [4]. Although this greatly improved the contrast in images, the information was still only qualitative.

B. Holography

The concept of holography was first proposed in 1948 by Dennis Gabor, a Hungarian-British physicist, for which he later won a Nobel prize in Physics in 1971 [5]. Holography is the process of recording the field scattered by an object onto a photographic plate so that a virtual image of the object can be reproduced in a different place and time without the original object being present. This is the optical version of a tape recording. Holography did not gain its popularity until the early 1960s after the invention of the laser, a highly coherent light source.

C. Early Applications

Holographic techniques found several applications in materials science. The Shack–Hartmann wavefront sensor (SHWFS) is widely known in the field of adaptive optics [6,7]. It was developed in the 1960s for characterizing the optical transfer function (OTF) of the atmosphere when measuring stars and satellites. After the related technologies became mature, SHWFS was applied for measuring the quality of laser beams, the roughness of semiconductor disks, and cornea profiles in ophthalmology. A typical SHWFS consists of a 2D array of identical lenses called lenslets. The wavefront under test is sampled by the lenslets. A uniform wavefront will be focused onto an equally spaced 2D grid on a photon sensor, e.g., a charge-coupled device (CCD) camera. However, if the wavefront has a slope before a lenslet, the focus will be shifted by an amount that is proportional to the slope. Thus, by measuring the shift of the focal spot on the photon sensor, the original wavefront can be reconstructed.

In the 1980s and 1990s, Wyant and co-workers made significant contributions in developing and commercializing interferometric technologies, such as computer-generated holography, phase-shifting interferometry, and white light interferometry [8–10]. Technology developed at Zygo Corporation also aims at optical testing using white light interferometry [11]. Initially, the interferometric instruments suffered from vibrational noise. To mitigate this problem, 4D technology detects 4 phase shifts simultaneously via a pixelated phase-mask [12].

D. Quantitative Phase Imaging

Advances in computers and CCDs in the 1990s enabled holograms to be recorded on CCD cameras, rather than photorefractive materials. The images could then be reconstructed digitally. Since the turn of the millennium, significant advances have been made in imaging and sensing technologies. High-quality CCD and complementary metal-oxide-semiconductor (CMOS) cameras are now available at relatively reasonable prices. As a result, an exciting new field, quantitative phase imaging (QPI), has emerged and found great success in the fields of materials and life sciences [13]. QPI utilizes the fact that the phase of a field is much more sensitive than its amplitude. As fields from the source interact with the specimen, phase shifts are induced in the scattered fields with respect to the unscattered light. These minute phase shifts contain the desired structural information about the sample under investigation. Unfortunately, visible frequencies are far too fast for conventional cameras or detectors to measure the phase shift directly. These devices can only measure intensity. Thus, a variety of modulation schemes have been employed to gain access to the phase.

Several different approaches to QPI exist, which can be best classified by the following category descriptors: common-path, phase-shifting, off-axis, and white light interferometry; each with their own strengths and weaknesses [13]. In general, common-path geometries are highly stable, since both arms of the interferometer overlap and experience highly correlated, nearly identical noise, which cancels out in the final phase measurement [13]. Some common-path methods include Fourier phase microscopy (FPM) [14], spatial light interference microscopy (SLIM), and diffraction phase microscopy (DPM) [15], as well as quadriwave lateral shearing interferometry (QWLSI) [16], spiral phase contrast [17], and transport of intensity [18,19]. Phase-shifting methods perform temporal phase modulation and require multiple raw images (3 or more) in order to reconstruct a single phase image. For this reason, phase-shifting methods are usually not used for high-speed dynamics [20]. Off-axis methods create modulation spatially, requiring only a single capture to produce a phase image. Most conventional digital holography (DH) methods use an off-axis approach [21–25]. Such methods are well-suited for single-shot imaging and high-speed measurements, but typically have higher noise than their common-path counterparts [15,22,23,25,26].

QPI has been performed using a variety of sources including lasers in both the visible and infrared (IR) regimes [27]. Broadband techniques using light emitting diodes (LEDs), super-continuum lasers, and standard halogen lamp illumination have also been demonstrated [20,28–30]. White light methods generally exhibit lower noise due to the lower coherence, both spatially and temporally, which reduces noise mechanisms such as laser speckle. However, when used with insufficient spatial coherence, white light may introduce object-dependent artifacts such as halos, which prevent proper reconstruction of the topography [20,29,30]. Both the spatial and temporal coherence of the source must be considered when performing any type of interferometry. For accurate QPI measurements, the mutual intensity function must be sufficiently flat over the area of the largest object being measured [29].

2. Diffraction Phase Microscopy

DPM combines many of the best attributes from various QPI techniques [15,31,32]. DPM utilizes a diffraction grating, 4*f* lens system, a pinhole filter (PF), and a CCD to create a compact Mach–Zehnder interferometer. This quasi-common-path configuration makes the approach single shot, meaning that the acquisition speed is limited only by the speed of the camera employed, while still benefiting from the noise cancellation properties of common-path interferometric systems. The DPM module is shown in Fig. 1 and can be placed at the output port of any conventional microscope.

DPM works as follows: a diffraction grating (G) is placed in the output image plane of the microscope (IP1). The periodic structure of the grating separates the imaging field into many copies of itself, which diffract from the grating at various angles, some of

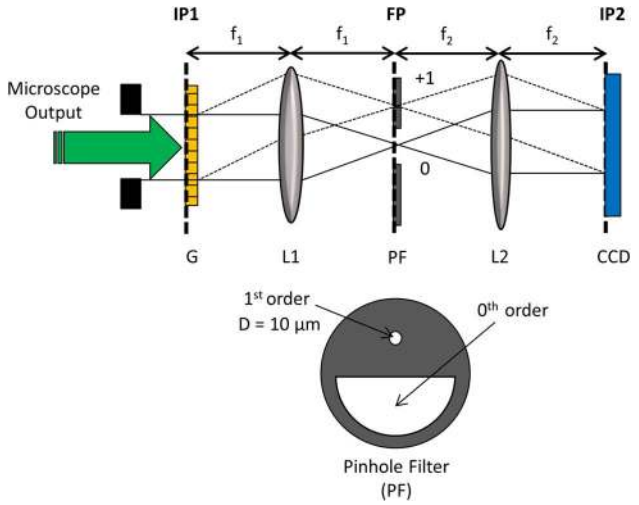

Fig. 1. Diffraction phase microscopy. A diffraction grating (G), pinhole filter (PF), and 4f lens system (L1,L2) are used to produce an interferogram on the CCD sensor. This spatially modulated signal contains the phase information which allows us to reconstruct the surface topography with nanometer accuracy. Adapted from [32].

which are captured by the first lens (L1). L1 is placed one focal length away from the grating, such that a Fourier plane (FP) is created a focal length behind the lens. A PF is placed in the FP and is used to block all orders except for the 0 and +1 orders. The zero order remains unfiltered and travels directly down the optical axis through the center of all lenses, minimizing the aberrations present in the final image. Meanwhile, the +1 order is filtered down using a small enough pinhole (10 μm for our design) such that after the second lens (L2) takes another Fourier transform, the field approaches a plane wave (i.e., uniform over the CCD sensor) and can serve as the reference of the interferometer. At the CCD sensor (IP2), the two fields interfere creating an interferogram, a spatially modulated signal containing the complete (phase and amplitude) imaging field information.

Figure 2 illustrates the procedure for taking the raw images captured by the CCD and processing them to get the final amplitude and phase image. Before imaging a new sample, a calibration image is taken on a flat, featureless portion of the sample. The calibration (or background) image is used to subtract the background. This procedure removes nonuniformities and noise in both the amplitude and phase that are invariant under shifts of the sample, as we will illustrate shortly. Once the background image is obtained, the sample can be imaged freely. If it is not possible to collect a calibration image, the curvature in both the amplitude and phase images must be removed using a curve-fitting program. This procedure does not remove the background noise. A typical background image is shown in Fig. 2(a). Figure 2(b) is a raw image of a micropillar, which is a cylindrical structure 60 μm in diameter and 110 nm in height. Since the grating is in a conjugate image plane, any scratches or defects on the grating will show up in focus and in identical locations in all images, as seen in Figs. 2(a) and 2(b). These will be removed during background subtraction. Figure 2(c) shows a zoomed-in portion of Fig. 2(a) where no shifts in the fringes are present, indicating no local variation in optical path length. Figure 2(d) shows a zoomed-in portion of the micropillar's edge. Note the clear shift in the fringes due to the step change in height. Figure 2(e) shows the Fourier transform of the raw interferogram. The semicircles are due to the physical shape of the filter shown in Fig. 1. A simple bandpass filter is used to pick out the spatially modulated signal [see Fig. 2(f)] and bring it back to baseband [Fig. 2(g)]. Once this is done, the amplitude and phase can be readily extracted.

Figures 3(a) and 3(b) show the computed height map and corresponding cross section of the micropillar control sample. The small peaks at the edges are due to missing high-frequency components not captured by the finite numerical aperture of the objective, sometimes referred to as the Gibbs phenomenon [29]. The height is proportional to the phase and depends on the mean wavelength of the illumination as well as the refractive index. The height can be computed as follows:

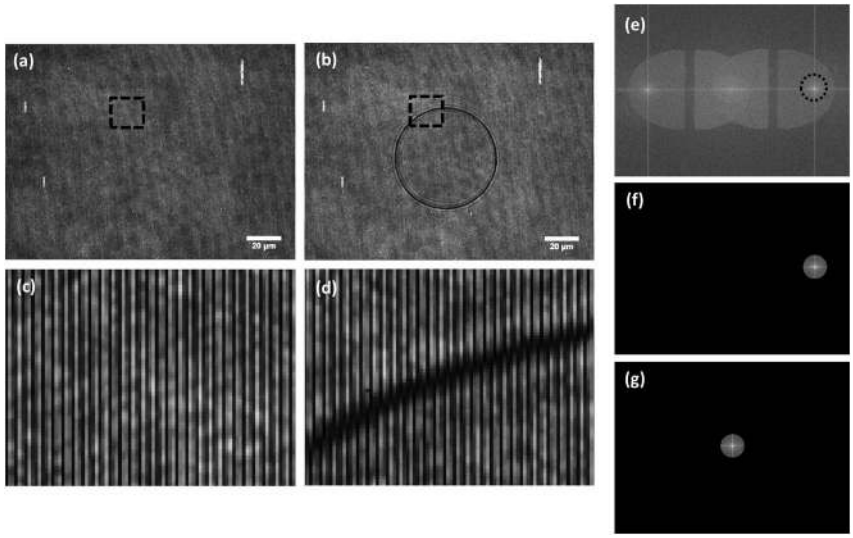

Fig. 2. DPM processing. (a) A calibration image. (b) A raw image of the micropillar. The scale bar in (a) and (b) is 20 μm. (c) The zoomed image taken from the dotted rectangle in (a) showing no shift in the fringes. (d) The zoomed image taken from the dotted rectangle in (b) showing a shift in the fringes due to the height change at the pillar's edge. (e) The Fourier transform of the raw image. (f) The modulated signal can be picked out using a bandpass filter and (g) brought back to baseband, where the phase can be extracted and used to reconstruct the surface topography. Adapted from [32].

$$h(x,y) = \frac{\varphi(x,y)\lambda_0}{2\pi\Delta n}, \tag{1}$$

where $\varphi(x,y)$ is the phase image, λ_0 is the mean free-space wavelength, and Δn is the refractive index difference between the structure of interest and its surrounding medium. This equation is valid for transmission, but in reflection, an additional factor of two is required to account for the fact that the light travels to the surface and back, i.e., replace h with $2h$. Due to the modulo 2π nature of the phase, phase unwrapping errors can occur for sharp edges that undergo a greater than 2π phase shift (π in reflection mode) across adjacent pixels. Phase unwrapping errors can be eradicated using numerical methods [33] or measurements with 2 or more wavelengths [34,35]. Note also, that in pure reflection, the light travels only in the surrounding medium, so Δn must be replaced with the refractive index of the surrounding medium, which is typically 1 for air. After computing the height, the background is set to zero. Also, notice that the scratches on the grating that were emphasized in Fig. 2 are now removed and the background is very clean. In fact, DPM provides spatial and temporal noise floors of about 0.55 and 0.4 nm, respectively [36]. These subnanometer noise levels were obtained by using a highly stable laser, properly diffusing the laser (rotating diffuser), and preventing multiple or back reflections (optical isolator).

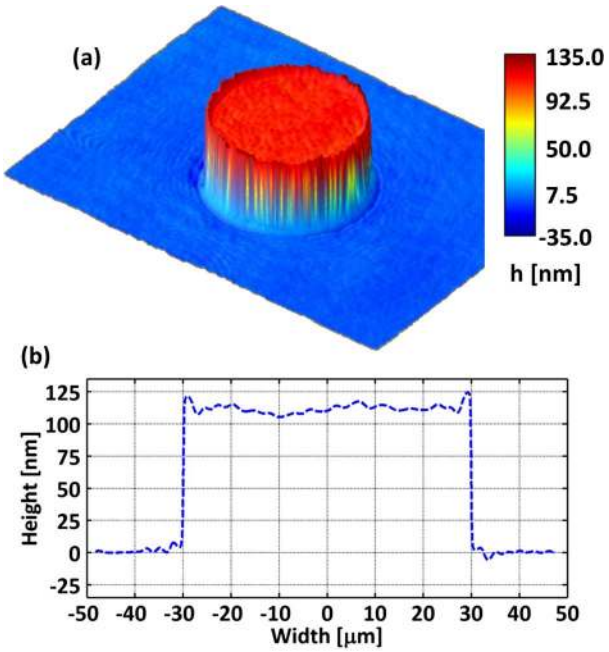

Fig. 3. Topographic profile obtained via DPM. (a) The height map and (b) corresponding cross section showing height and diameter of the measured micropillar. Adapted from [32].

3. Materials Science Applications

A. Watching Semiconductors Etch

DPM allows us to watch semiconductors as they etch [31]. In order to illustrate these capabilities, an oxide mask containing the University of Illinois logo was patterned onto an $n+$ GaAs wafer. A dilute solution of 1:1:50 H_3PO_4:H_2O_2:H_2O was used to create heterogeneities in the etch which could be quantified using our technique. Figures 4(a)–4(d) contain still images from our epi-DPM etch depth tracker. A video was collected at 8.93 frames/s using a 5× objective to monitor the etch, resulting in a 320 μm × 240 μm field of view (FOV). Figures 4(a)–4(d) show the spatially resolved etch depths at 0, 15, 30, and 45 s, respectively. Here, we must assume that there are no large local variations in the refractive index of

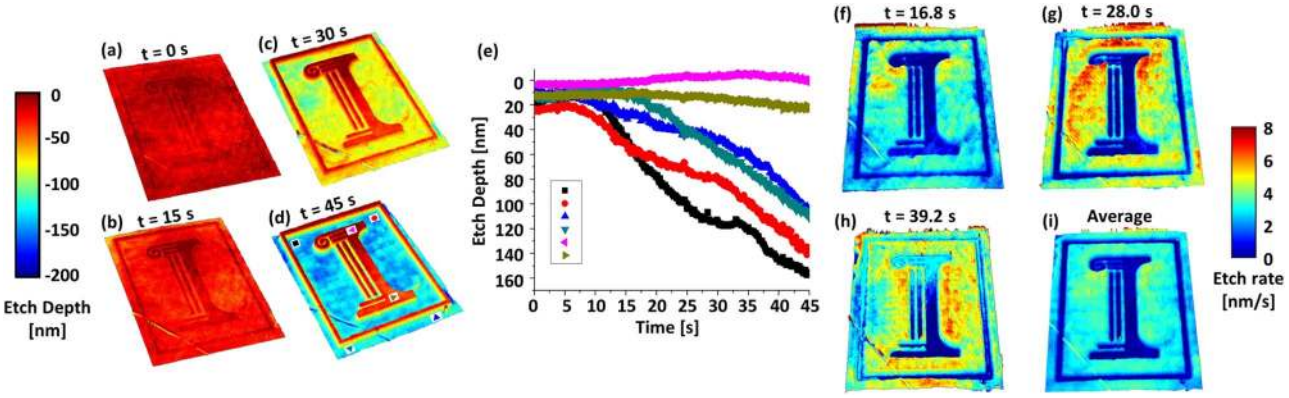

Fig. 4. Watching semiconductors etch. DPM allows us to watch semiconductors as they etch, tracking the instantaneous etch depths and etch rates at each pixel throughout the entire process. A 5× objective was used for monitoring the etch, resulting in a FOV of 320 μm × 240 μm for each of the images shown. The video was acquired at 8.93 frames/s for 45 s. (a)–(d) Still frames at 0, 15, 30, and 45 s, respectively, are displayed showing the time evolution of the etch depth. (e) Time-resolved etch depths at points indicated in (d). (f)–(h) Instantaneous etch rates at frame 150 (16.8 s), 250 (28.0 s), and 350 (39.2 s). (i) The etch rate averaged over the entire process. Adapted from [31].

the medium, which is a valid assumption given the diluteness of the solution and the minute volumes of material being etched compared to the amount of liquid in the dish. Figure 4(e) plots the time-resolved etch depths at selected locations indicated in Fig. 4(d). Fluctuations in both the etch depth and etch rates can be observed at various locations simultaneously. By obtaining the height at each pixel at each frame, we are also able to track the instantaneous etch rates throughout the entire etching process. Figures 4(f)–4(h) show the etch rates at various times throughout the process, revealing the nonuniformities in the etch. Figure 4(i) shows the overall etch rate, i.e., averaged over the entire process. Although the etch rates may vary dramatically over the FOV at any given time, the etch rates tend to average out as the process continues. This new development provides the technology required to create a new multiuser cleanroom tool for wet etching that will allow the user to observe all of this information during etching, make on-the-fly adjustments to the recipe, and have full control over the process. This will greatly reduce the number of iterations required in optimizing a recipe and naturally improve the overall yield.

B. Digital Projection Photochemical Etching

Our lab has also developed a new fabrication technique called digital projection photochemical etching, where an image from a digital projector is focused onto the sample's surface and the light itself defines the etching pattern [31,36]. This completely eliminates the need for spin coating photoresist, aligning, exposing, and developing as in conventional photolithography. The projected light pattern interacts with the sample and excites minority carriers which diffuse to the surface and provide additional energy to catalyze the etching process. This technique has been used successfully to etch complicated gray-scale structures in a single etching step, a feat difficult to accomplish using conventional lithography [31,36]. Figure 5(a) shows an example of a typical projected image. This particular mask uses green light with gray levels of 0, 60, and 78. The pattern was chosen to create a multilevel structure with widths of 75 and 150 μm. A 33 s etch was then performed in order to produce heights of 0, 50, and 100 nm. An epi-DPM height map of the etched structure along with its histogram are laid out in Figs. 5(b) and 5(c). Figure 5(d) shows the surface topography of a photochemical- (PC) etched Archimedean spiral with a maximum height of 100 nm, illustrating our ability to precisely etch gray-scale structures. Again, this was done in a single 33 s etch step. Using standard lithography would require the spiral to be broken up into discrete steps, each requiring its own series of processing steps. Figure 5(e) contains the height map of a microlens array. The pitch and diameter are 120 and 100 μm, respectively. All three structures depicted in this section where etched using $1:1:50$ $H_3PO_4:H_2O_2:H_2O$ on $n+$ GaAs wafers. The intensity and wavelength (color) of the projected pattern can also be adjusted in real-time granting both spatial and material selectivity in a dynamic fashion. Furthermore, by integrating the PC etching system into the existing diffraction phase microscope (epi-DPM), we are able to characterize our PC-etched structures on site in a completely noninvasive and nondestructive manner [36]. This, of course, is not possible with scanning electron microscopy (SEM), transmission electron microscopy (TEM), atomic force microscopy (AFM), or other similar inspection methods.

C. Microdroplet Evaporation

Among the few methods currently available to characterize surface wetting and evaporation, the goniometric technique for sessile drops is widely used [37,38]. This approach uses a high-speed, high-resolution camera along with image analysis software to capture a side-view of the droplet during evaporation. The scheme can provide accurate height information about the drop profile; however, it relies heavily on geometrical approximations to derive the

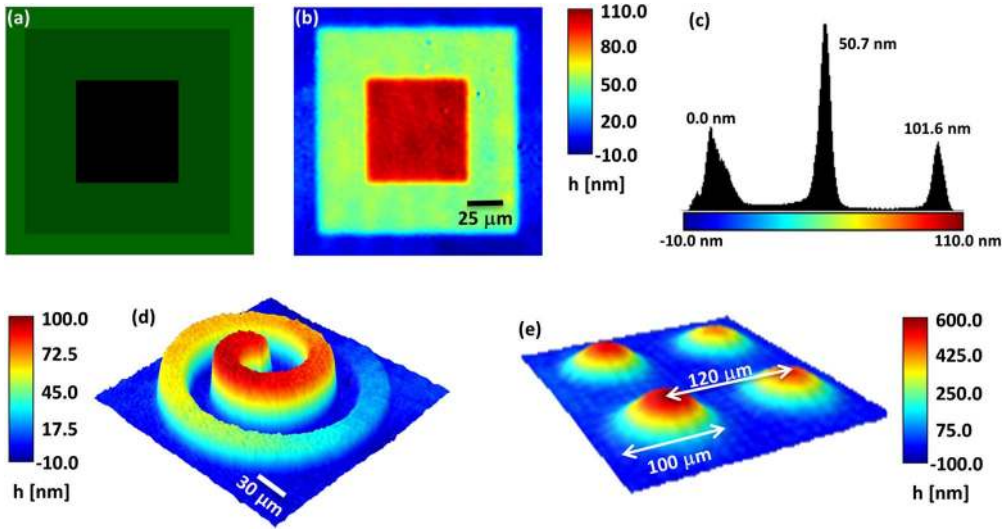

Fig. 5. Digital projection photochemical etching. This technique has been used successfully to etch complicated gray-scale structures in a single etching step, which are typically very difficult or expensive to fabricate with conventional lithography. (a) An image from the digital projector focused onto the sample's surface and used to define the etching pattern. The projected image used gray levels of 0, 60, and 78 and a single photochemical etch was performed for 33 s resulting in mean heights of 0, 50.7, and 101.6 nm. The mask geometry, gray levels, and etch time were calibrated to produce a multilevel structure with widths of 150 and 75 μm and heights of 0, 50, and 100 nm. (b) The DPM height map of stacked cubes. (c) The histogram of the image in (b) showing the heights of the three levels. (d) The topographical profile of the PC-etched Archimedean spiral produced in a single etch step. (e) The topographical reconstruction of the microlens array fabricated using PC etching showing diameter and pitch. Adapted from [31,36].

other essential droplet parameters. Most importantly, since the method is limited to a single viewing angle, observations of spatial heterogeneities and other interesting phenomena that occur during the evaporation process are somewhat limited. In addition, such techniques have had difficulty resolving small contact angles (<10°) and, more broadly, small (micrometer-sized) droplets in general.

In contrast to contemporary methods, DPM provides a full 3-dimensional (3D) description of the droplet's shape during evaporation without *a priori* assumptions about its geometry. This capability enables spatially and temporally resolved measurements of the height, contact radius, contact angle, volume, surface area, and mass flux density (MFD). With all of this information at our disposal, we are able to directly observe a variety of phenomena that occur during droplet evaporation, including nonuniformities in the contact angle, time-dependent and heterogeneous pinning and depinning, as well as the effects of neighboring droplets on drying dynamics. The characterization of surface wetting and evaporation is important for applications including thin-film deposition, microlens fabrication, self-assembly of nanoparticles, inkjet printing, and printable electronics [39]. DPM provides a noninvasive, nondestructive method for monitoring such processes in real-time.

Figure 6(a) shows the 3D profile of an evaporating deionized (DI) water microdroplet on a transparent glass substrate imaged in transmission. By taking the gradient, thresholding, and masking, the contact angle at each pixel around the droplet's perimeter can be measured during evaporation. Figure 6(b) shows a map of the contact angles from the droplet in Fig. 6(a). As a result of partial-pinning, the contact angles on the left side differ from those on the right. The histogram of contact angles provides an abundance of statistical information about the process and is shown in the inset. Figure 6(c) shows the time evolution of the average contact angle; the droplet is captured as it depins and transitions from the constant contact area mode (I) to the constant contact angle mode (II). The data are compared to the spherical cap approximation (SCA). Since we know the height associated with each pixel at each instant in time, it is possible to compute the MFD at each pixel during the entire process. The MFD is defined as the change in mass per unit area per unit time, and includes the effects of diffusive evaporation as well as radial convection within the droplet. Interestingly, we see in Fig. 6(d) that the presence of a neighboring droplet in the lower left-hand corner affects the local evaporation rate of the central droplet. This phenomenon is very difficult to observe with conventional techniques [40].

D. Dissolution of Biodegradable Electronic Materials

In the same way that dissolvable sutures disintegrate over the course of several weeks without requiring further surgery to remove, electronic devices have been fabricated using a variety of materials, which upon implantation into the body, dissolve over time without creating harmful by-products in the process. These devices have been shown to perform adequately over a given time-span and then degrade quickly, resorbing into the body after their function is complete [41].

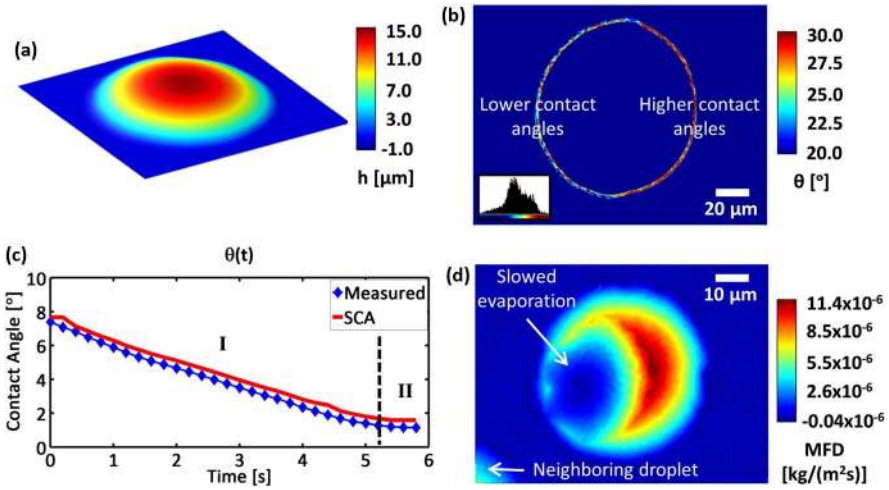

Fig. 6. Characterization of microdroplet evaporation using DPM. (a) A 3D profile of the evaporating microdroplet. (b) A map of the contact angles around the droplet's perimeter with a histogram showing their distribution. As a result of partial-pinning, the contact angles on the left side differ from those on the right. (c) Time evolution of the average contact angle showing the transition from the pinned (I) to depinned (II) mode until complete evaporation. A comparison is made to predictions of the SCA. (d) The MFD of the evaporating microdroplet. Notice that the presence of a second droplet in the lower-left corner affects the local evaporation rate. Such a phenomenon is difficult to observe with conventional techniques.

In the past, the development of biodegradable electronics was approached either by using water-soluble organic materials as the constituents [42,43] or by using nontransient electronic elements on bioresorbable substrates [44,45]. Recent progress exploits high-performance single crystalline silicon nanomembranes (Si NMs) as semiconducting materials, Mg as the conductors, MgO or SiO_2 for the gate/interlayer dielectrics, and silk for the packaging/substrate components [41]. All of these constituents are water-soluble and do not create any harmful byproducts upon dissolution. Furthermore, Si-based electronics have much better performance than their organic counterparts.

In order to provide accurate, quantitative dynamic height information, the epi-DPM imaging system was used to record several images throughout the dissolution process [46]. The samples were prepared from silicon-on-insulator (SOI) wafers that consist of the top Si layer, a buried oxide layer (SiO_2), and the bottom Si handle wafer. First, a periodic array of tiny circles was patterned on the surface of the top Si layer. To deliver the top Si NMs, hydrochloric acid (HF) was used to undercut the underlying buried oxide (SiO_2). The top layer of Si was then transfer-printed onto a spin cast film of SU-8 on glass substrate. The "UIUC" initials seen in Fig. 7 were then created using standard photolithography and by etching through the top Si layer down to the glue layer. Thus, the Si layer forming the "UIUC" initials was 100 nm in height. The letters were approximately 75 μm in length (top to bottom). The lines forming each letter were approximately 15 μm in width. The samples were placed into bovine serum in an incubator at body temperature (37°C). The dissolution rate increases with increasing temperature as well as increasing pH level of the medium. The samples were removed every 8 h for imaging. They were stored in a fresh solution of PBS in a clean container and returned to the incubator directly after imaging was complete. This avoids issues with contamination which have a mild effect on the dissolution rate.

Figures 7(a)–7(d) show 3D topographic images of the University of Illinois logo at 4 different stages of the dissolution process. The initial image was taken using the epi-DPM system and compared to values obtained using the Alpha Step IQ Profilometer. The mean heights were measured to be 97 nm in both cases. Images were then taken every 8 h using epi-DPM. Figure 7(e) shows the cross-sectional profiles that correspond to the images in Figs. 7(a)–7(d). The cross sections were taken long ways down the center of the "I" in "UIUC." The widths were measured to be 75 μm to within the resolution of the system, which is about 5 μm using the 5× objective. Note that we typically image much smaller features with higher magnification and NA objectives, giving us much better resolution. For instance, using any objective with an NA > 0.5 gives us submicrometer resolution. The heights at 0, 8, 16, and 24 h were 97 ± 2.1 nm, 67 ± 2.9 nm, 31 ± 1.9 nm, and 0 ± 0.7 nm, respectively. The dissolution rate is known to be nonlinear but seems to be quite repeatable given similar conditions.

We plan to image the dissolution behavior of other materials currently being used in applications for dissolvable electronics in a variety of media and to capture the resorption of electronic devices in their entirety.

E. Palladium Expansion

Palladium is known to readily react with hydrogen gas, resulting in changes in the optical, electronic, and material properties of the metal [47]. Based on these changes, a wide variety of optical hydrogen

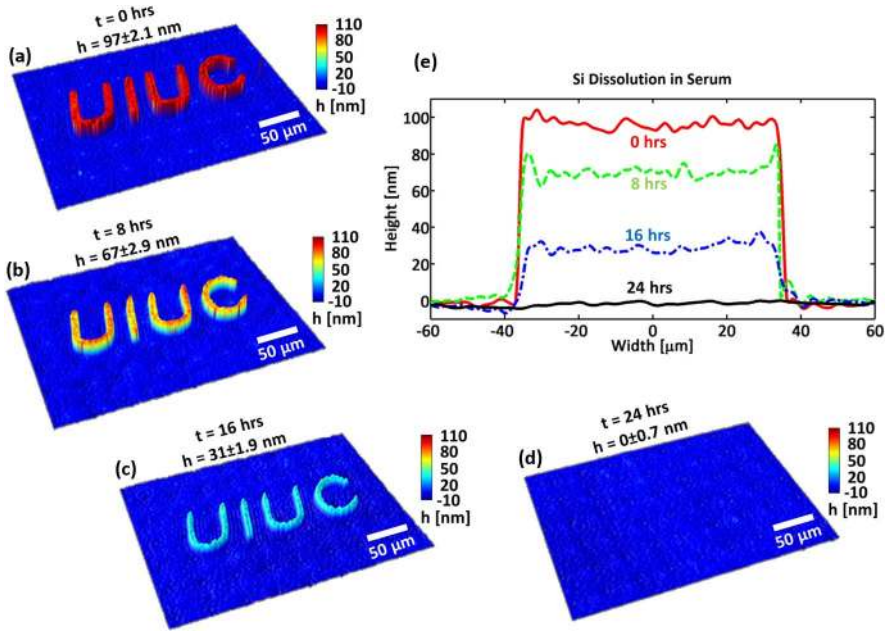

Fig. 7. Dissolution of biodegradable electronic materials. Dissolution of Si in serum. (a)–(d) The 3D topographic profiles of Si during dissolution at 0, 8, 16, and 24 h. (e) The cross-sectional profiles showing heights at various times in the dissolution process. The measured heights are 97 nm (0 h), 67 nm (8 h), 31 nm (16 h), and 0.0 nm (24 h). The dissolution process is not perfectly linear. The 97 nm layer completely dissolves within 24 h. Adapted from [46].

sensors have been proposed and studied [48,49]. In addition to being hazardous and used or produced in a wide variety of industries, hydrogen offers one solution to the rising demand for renewable and environmentally friendly fuel sources. For these reasons, there is considerable interest in building more accurate, faster, and more reliable hydrogen sensors. To assist in the design and modeling of these sensors, DPM was used to quantify the structural changes in Pd thin-films with hydrogen incorporation, an effect known as hydrogen-induced lattice expansion (HILE) [50].

Palladium micropillar samples were fabricated on an SiO2 substrate using a shadow mask lift off technique. The shadow mask consisted of 200 μm diameter holes and was placed in contact with the substrate for the deposition of a 300 nm Pd layer. After removing the mask, a second blanket layer of 40 nm Pd was deposited on the entire sample. This was done so that changes in the complex refractive index of Pd with hydrogen would not produce localized phase shifts, which would affect the measured height change. Both depositions were done via electron beam evaporation. The topography and cross section of one of the micropillars are shown in Figs. 8(a) and 8(b), respectively. The initial (prehydrogen exposure) height for this set of samples was measured to be 294 nm and the diameter was 200 μm.

A stainless steel flow chamber was machined and connected to mass flow controllers for measurements [50]. The measurements consisted of step pulses of hydrogen gas in nitrogen ambient, while the average pillar height was monitored. The total flow rate was kept constant at 300 sccm. Figure 8(c) shows the temporal stability of a calibration measurement during a nitrogen purge. The measured noise had a root mean square (rms) value of 0.26 nm. The time response of one of the Pd micropillars to a 90 min 0.5% hydrogen pulse is shown in Fig. 8(d). Exposure to hydrogen resulted in a measured average height change of 2.71 nm, or approximately a 0.92% increase in height due to lattice expansion. After purging the sample in nitrogen again for several hours the height returned to its initial value, within the error of the measurement.

By repeating this measurement for various hydrogen concentrations, substrates, and adhesion layers, this measurement will allow for more accurate and complete simulation and design of thin-film Pd-based sensors, which may behave differently than bulk palladium.

F. Semiconductor Wafer Defect Inspection

In-line detection of killer defects in a patterned silicon wafer is a grand challenge of the International Technology Roadmap for Semiconductors (ITRS). SEM and AFM are typically used for wafer defect inspection [51–53]. However, those methods have low throughput and can potentially damage the wafer, making them unsuitable for in-line wafer inspection. Optical microscopy is a nondestructive technique with high throughput, since it has a large FOV and needs no contact or sample preparation. Although the lateral resolution of an optical system is diffraction-limited to be of the order of $\lambda/2$, the performance of a defect inspection system is actually limited by the noise.

To overcome the noise issue, we built a highly sensitive detection system using an epi-DPM system with a 532 nm laser and an objective

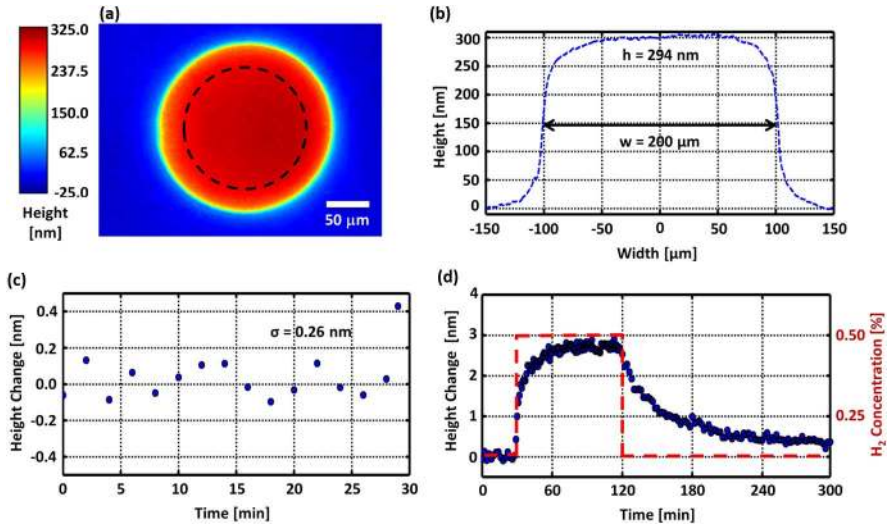

Fig. 8. Hydrogen-induced lattice expansion of palladium thin-films for hydrogen sensing applications. (a) A DPM image of the test structure before exposure. (b) A cross section showing initial dimensions. (c) The stability of height measurement during the N_2 baseline run on the micropillar. (d) 90 min of H_2 at 0.5% causes 2.71 ± 0.13 nm of material deformation.

with numerical aperture of NA = 0.9. The lateral resolution is diffraction-limited to be about $1.22\lambda/(\mathrm{NA}_{\mathrm{objective}} + \mathrm{NA}_{\mathrm{condenser}}) = 720$ nm, where $\mathrm{NA}_{\mathrm{condenser}} = 0$ for collimated illumination, according to the Rayleigh criterion. The FOV of the system is 30 by 27 μm. We used this system to inspect a 22 nm node intentional defect array (IDA) wafer. A defect-free portion of the IDA wafer is shown in Fig. 9(a). The silicon wafer has a pattern that consists of 22 nm wide lines of polysilicon that are 120 or 260 nm long and 110 nm tall. The lines form a periodic structure with a 0.8 by 0.8 μm square as the unit cell. The unit cell is repeated to form a 100 by 100 μm 2D defect array with a rhombic lattice pattern. A zoomed-in portion of the defect-free pattern is shown in Fig. 9(b). A parallel (red) bridge defect is shown in Fig. 9(c). This defect is located in the center of the defect array. In the following, we show the process of detecting this type of defect.

Despite our low-noise common-path interferometer, the deep subwavelength defect cannot be detected with our system in a single-shot image due to the residual noise. Thus, to remove the noise, a sequence of interferograms is acquired by translating the wafer in the direction parallel to the underlying line structure. For each interferogram, we retrieve a phase and an amplitude image. With the acquired image sequences, we developed an image postprocessing method to remove different types of noise and system imperfections to achieve defect detection. The method includes second-order frame difference, image stitching, and matched defect pattern convolution (2DISC); see more details in reference [54]. With 2DISC processing, we produce a panoramic second-order difference image and a matched defect pattern convolution image for phase and amplitude, respectively. Here, we show the detection results for a defect array with a 20 nm wide by 160 nm long by 110 nm tall parallel bridge defect. The panoramic second-order difference phase and amplitude image of this defect array are shown in Figs. 10(a) and 10(b), respectively. The size of the panoramic image is 70 by 27 μm. In the center of the panoramic image, the defect signal can be clearly identified. However, there is still undesired underlying structure, which reduces the detectability. To remove the underlying structure and extract the defect signal, we convolve the image with a matched filter pattern, i.e., a tripole pattern with a Gaussian profile for each lobe. The matched filtering technique was also used in Fresnel particle tracing in 3D with DPM [55]. The Gaussian profile has a 360 nm width to maximize the defect extract signal. After convolution, 2DISC phase and amplitude images are created as shown in Figs. 10(c) and 10(d), respectively. In both 2DISC images, the defect signal-to-background contrast has been significantly improved, compared with Figs. 10(a) and 10(b). To quantitatively study the enhancement with the image postprocessing, we use the peak-signal-to-noise-ratio (PSNR), defined in reference [54]. It is found that the PSNR

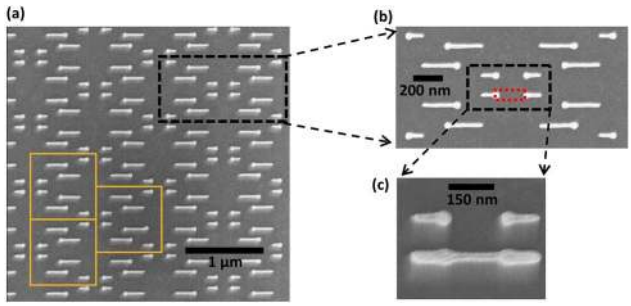

Fig. 9. SEM images illustrate the printed defects in the 22 nm node IDA wafer. (a) A defect-free portion of the wafer pattern with unit cells labeled in orange boxes. (b) A zoomed-in portion of the pattern, where the location of a parallel bridge defect is marked by a red box. (c) Illustration of a parallel bridge defect. Adapted from [54].

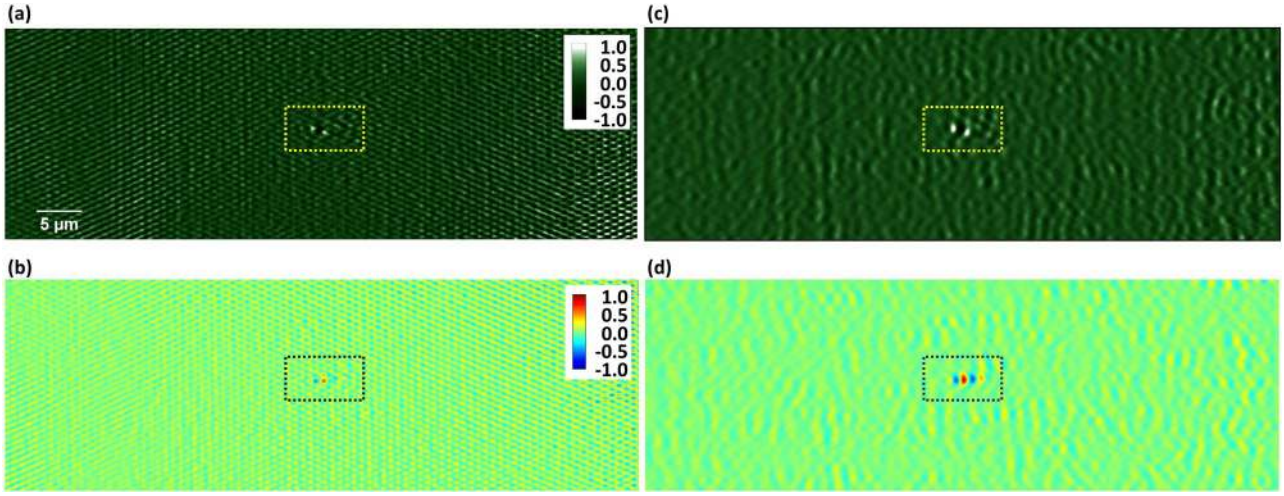

Fig. 10. Illustration of the 2DISC image postprocessing method for enhancing defect detection. (a) and (b) Panoramic second-order difference phase and amplitude images, respectively. (c) and (d) 2DISC amplitude and phase images, respectively. For each image, the location of the defect is marked by a color rectangular box. All values are normalized and represented by arbitrary units (a.u.). Adapted from [54].

has improved by about 20 dB by comparing the raw image with the 2DISC images for both phase and amplitude. The image postprocessing parameters are optimized, with detailed verifications in the supplementary section of reference [54]. Submatrix processing can also be applied to the 2DISC image for further accessing the defect. More recently, we enhanced the system sensitivity by performing 3D wafer scanning with a white light source as the illumination and successfully detected defects in a 9 nm node wafer [56].

4. Summary and Outlook

Quantitative phase imaging in general and DPM in particular, has been met with growing success in the recent years. Its compact design and robust performance allow it to accurately monitor nanoscale dynamics in a wide variety of environments. It is currently being used to monitor etching dynamics [31], photochemical etching [31,36], microdroplet evaporation, dissolution of biodegradable electronic materials [46], and the expansion and deformation of thin-films [50]. It has also found applications in defect detection for semiconductor wafers [36,54,56].

Recent developments have led to white light versions of DPM [30], which commonly result in lower noise floors. This is a result of lower coherence, both temporally and spatially, which reduces some noise mechanisms such as speckle. Unfortunately, white light systems with low spatial coherence also exhibit object-dependent artifacts like the halo effect which may disrupt the quantitative measurement [29]. Recently, we have shown that halo and shade-off are one and the same, a high-pass filtering phenomenon caused by limited spatial coherence and that a PF in the condenser aperture or a supercontinuum laser source can be used to achieve the necessary spatial coherence for obtaining quantitatively correct height maps [29]. The broadband nature of white light sources provides added potential for spectroscopic and tomographic applications. With white light DPM now capable of halo-free imaging [29], we expect this technique will continue to find new and exciting applications in a wide variety of fields.

This work is supported by a NSF CBET-1040462 MRI award with matching funds from the University of Illinois and also by the Semiconductor Research Corporation (contract P13117).

References

1. J. van Zuylen, "The microscopes of Antoni van Leeuwenhoek," J. Microsc. **121**, 309–328 (1981).
2. E. Abbe, "Beitrage zur Theorie des Mikroscps und der mikrskopischen Wahrnehmung," Archiv fuer Mikroskopische Anatomie und Entwicklungsmechanik **9**, 413–418 (1873).
3. F. Zernike, "How I discovered phase contrast," Science **121**, 345–349 (1955).
4. G. Normarski, "Microinterferometre differentiel a ondes polarisees," J. Phys. Radium **16**, 9S–11S (1955).
5. D. Gabor, "A new microscopic principle," Nature **161**, 777–778 (1948).
6. B. C. Platt and R. Shack, "History and principles of Shack–Hartmann wavefront sensing," J. Refract. Surg. **17**, S573–S577 (2001).
7. J. Primot, "Theoretical description of Shack–Hartmann wavefront sensor," Opt. Commun. **222**, 81–92 (2003).
8. A. J. Macgover and J. C. Wyant, "Computer generated holograms for testing optical elements," Appl. Opt. **10**, 619–624 (1971).
9. J. C. Wyant, "Use of an ac heterodyne lateral shear interferometer with real-time wavefront correction systems," Appl. Opt. **14**, 2622–2626 (1975).
10. B. Bhushan, J. C. Wyant, and C. L. Koliopoulos, "Measurement of surface-topography of magnetic tapes by Mirau interferometry," Appl. Opt. **24**, 1489–1497 (1985).
11. P. Degroot and L. Deck, "Surface profiling by analysis of white-light interferograms in the spatial-frequency domain," J. Mod. Opt. **42**, 389–401 (1995).
12. J. E. Millerd, N. J. Brock, J. B. Hayes, M. B. North-Morris, M. Novak, and J. C. Wyant, "Pixelated phase-mask dynamic interferometer," Proc. SPIE **5531**, 304–314 (2004).
13. G. Popescu, *Quantitative Phase Imaging of Cells and Tissues* (McGraw-Hill, 2011).
14. G. Popescu, L. P. Deflores, J. C. Vaughan, K. Badizadegan, H. Iwai, R. R. Dasari, and M. S. Feld, "Fourier phase microscopy for investigation of biological structures and dynamics," Opt. Lett. **29**, 2503–2505 (2004).

15. G. Popescu, T. Ikeda, R. R. Dasari, and M. S. Feld, "Diffraction phase microscopy for quantifying cell structure and dynamics," Opt. Lett. **31**, 775–777 (2006).
16. P. Bon, G. Maucort, B. Wattellier, and S. Monneret, "Quadriwave lateral shearing interferometry for quantitative phase microscopy of living cells," Opt. Express **17**, 13080–13094 (2009).
17. S. Bernet, A. Jesacher, S. Fürhapter, C. Maurer, and M. Ritsch-Marte, "Quantitative imaging of complex samples by spiral phase contrast microscopy," Opt. Express **14**, 3792–3805 (2006).
18. A. Barty, K. A. Nugent, D. Paganin, and A. Roberts, "Quantitative optical phase microscopy," Opt. Lett. **23**, 817–819 (1998).
19. T. E. Gureyev and K. A. Nugent, "Rapid quantitative phase imaging using the transport of intensity equation," Opt. Commun. **133**, 339–346 (1997).
20. Z. Wang, L. Millet, M. Mir, H. Ding, S. Unarunotai, J. Rogers, M. U. Gillette, and G. Popescu, "Spatial light interference microscopy (SLIM)," Opt. Express **19**, 1016–1026 (2011).
21. J. Kühn, F. Charrière, T. Colomb, E. Cuche, F. Montfort, Y. Emery, P. Marquet, and C. Depeursinge, "Axial subnanometer accuracy in digital holographic microscopy," Meas. Sci. Technol. **19**, 074007 (2008).
22. F. Charrière, J. Kühn, T. Colomb, F. Montfort, E. Cuche, Y. Emery, K. Weible, P. Marquet, and C. Depeursinge, "Characterization of microlenses by digital holographic microscopy," Appl. Opt. **45**, 829–835 (2006).
23. P. Ferraro, S. Grilli, D. Alfieri, S. De Nicola, A. Finizio, G. Pierattini, B. Javidi, G. Coppola, and V. Striano, "Extended focused image in microscopy by digital holography," Opt. Express **13**, 6738–6749 (2005).
24. B. Kemper and G. von Bally, "Digital holographic microscopy for live cell applications and technical inspection," Appl. Opt. **47**, A52–A61 (2008).
25. T. Colomb, S. Krivec, H. Hutter, A. A. Akatay, N. Pavillon, F. Montfort, E. Cuche, J. Kühn, C. Depeursinge, and Y. Emery, "Digital holographic reflectometry," Opt. Express **18**, 3719–3731 (2010).
26. T. Ikeda, G. Popescu, R. R. Dasari, and M. S. Feld, "Hilbert phase microscopy for investigating fast dynamics in transparent systems," Opt. Lett. **30**, 1165–1167 (2005).
27. B. Joshi, I. Barman, N. C. Dingari, N. Cardenas, J. S. Soares, R. R. Dasari, and S. Mohanty, "Label-free route to rapid, nanoscale characterization of cellular structure and dynamics through opaque media," Sci. Rep. **3**, 1–8 (2013).
28. J. A. Rodrigo and T. Alieva, "Rapid quantitative phase imaging for partially coherent light microscopy," Opt. Express **22**, 13472–13483 (2014).
29. C. Edwards, B. Bhaduri, T. Nguyen, B. Griffin, H. Pham, T. Kim, G. Popescu, and L. L. Goddard, "Effects of spatial coherence in diffraction phase microscopy," Opt. Express **22**, 5133–5146 (2014).
30. B. Bhaduri, H. Pham, M. Mir, and G. Popescu, "Diffraction phase microscopy with white light," Opt. Lett. **37**, 1094–1096 (2012).
31. C. Edwards, A. Arbabi, G. Popescu, and L. L. Goddard, "Optically monitoring and controlling nanoscale topography during semiconductor etching," Light Sci. Appl. **1**, 1–6 (2012).
32. B. Bhaduri, C. Edwards, H. Pham, R. Zhou, T. Nguyen, L. Goddard, and G. Popescu, "Diffraction phase microscopy: principles and applications in materials and life sciences," Adv. Opt. Photon. **6**, 57–119 (2014).
33. H. Pham, H. Ding, N. Sobh, M. Do, S. Patel, and G. Popescu, "Off-axis quantitative phase imaging processing using CUDA: toward real-time applications," Biomed. Opt. Express **2**, 1781–1793 (2011).
34. C. J. Mann, P. R. Bingham, V. C. Paquit, and K. W. Tobin, "Quantitative phase imaging by three-wavelength digital holography," Opt. Express **16**, 9753–9764 (2008).
35. M. T. Rinehart, N. T. Shaked, N. J. Jenness, R. L. Clark, and A. Wax, "Simultaneous two-wavelength transmission quantitative phase microscopy with a color camera," Opt. Lett. **35**, 2612–2614 (2010).
36. C. Edwards, K. Wang, R. Zhou, B. Bhaduri, G. Popescu, and L. L. Goddard, "Digital projection photochemical etching defines gray-scale features," Opt. Express **21**, 13547–13554 (2013).
37. P. J. Yunker, T. Still, M. A. Lohr, and A. G. Yodh, "Suppression of the coffee-ring by shape-dependent capillary interactions," Nature **476**, 308–311 (2011).
38. P. J. Yunker, M. Gratale, M. A. Lohr, T. C. Lubensky, and A. G. Yodh, "Influence of particle shape on bending rigidity of colloidal monolayer membranes and particle deposition during droplet evaporation in confined geometries," Phys. Rev. Lett. **108**, 228303 (2012).
39. H. Y. Erbil, "Evaporation of pure liquid sessile and spherical suspended drops: a review," Adv. Colloid Interface Sci. **170**, 67–86 (2012).
40. R. D. Deegan, O. Bakajin, T. F. Dupont, G. Huber, S. R. Nagel, and T. A. Witten, "Contact line deposits in an evaporating drop," Phys. Rev. E **62**, 756–765 (2000).
41. S.-W. Hwang, H. Tao, D.-H. Kim, H. Cheng, J.-K. Song, E. Rill, M. A. Brenckle, B. Panilaitis, S. M. Won, Y.-S. Kim, Y. M. Song, K. J. Yu, A. Amee, R. Li, Y. Su, M. Yang, D. L. Kaplan, M. R. Zakin, M. J. Slepian, Y. Huang, F. G. Omenetto, and J. A. Rogers, "A physically transient form of silicon electronics," Science **337**, 1640–1644 (2012).
42. C. J. Bettinger and Z. Bao, "Organic thin-film transistors fabricated on resorbable biomaterial substrates," Adv. Mater. **22**, 651–655 (2010).
43. M. Irimia-Vladu, P. A. Troshin, M. Reisinger, L. Shmygleva, Y. Kanbur, G. Schwabegger, M. Bodea, R. Schwödiauer, A. Mumyatov, J. W. Fergus, V. F. Razumov, H. Sitter, N. S. Sariciftci, and S. Bauer, "Biocompatible and biodegradable materials for organic field-effect transistors," Adv. Funct. Mater. **20**, 4069–4076 (2010).
44. D.-H. Kim, Y.-S. Kim, J. Amsden, B. Panilaitis, D. L. Kaplan, F. G. Omenetto, M. R. Zakin, and J. A. Rogers, "Silicon electronics on silk as a path to bioresorbable, implantable devices," Appl. Phys. Lett. **95**, 133701 (2009).
45. D.-H. Kim, J. Viventi, J. J. Amsden, J. Xiao, L. Vigeland, Y.-S. Kim, J. A. Blanco, B. Panilaitis, E. S. Frechette, D. Contreras, D. L. Kaplan, F. G. Omenetto, Y. Huang, K.-C. Hwang, M. R. Zakin, B. Litt, and J. A. Rogers, "Dissolvable films of silk fibroin for ultrathin conformal bio-integrated electronics," Nat. Mater. **9**, 511–517 (2010).
46. S. Hwang, G. Park, C. Edwards, E. A. Corbin, S. Kang, H. Cheng, J. Song, J. Kim, S. Yu, J. Ng, J. E. Lee, C. Yee, B. Bhaduri, Y. Su, F. G. Omenetto, Y. Huang, R. Bashir, L. L. Goddard, G. Popescu, K.-M. Lee, and J. A. Rogers, "Dissolution chemistry and biocompatibility of single crystalline silicon nanomembranes and associated materials for transient electronics," ACS Nano **8**, 5843–5851 (2014).
47. T. Flanagan and W. A. Oates, "The palladium-hydrogen system," Annu. Rev. Mater. Sci. **21**, 269–304 (1991).
48. B. G. Griffin, A. Arbabi, A. M. Kasten, K. D. Choquette, and L. L. Goddard, "Hydrogen detection using a functionalized photonic crystal vertical cavity laser," IEEE J. Quantum Electron. **48**, 160–168 (2012).
49. S. McKeown and L. Goddard, "Hydrogen detection using polarization diversity via sub-wavelength fiber aperture," IEEE Photon. J. **4**, 1752–1761 (2012).
50. C. Edwards, S. J. McKeown, J. Zhou, G. Popescu, and L. L. Goddard, "Observing hydrogen induced deformations in palladium thin-films," in *IEEE Photonics Conference* (IEEE, 2013), pp. 612–613.
51. J. Goldstein, *Scanning Electron Microscopy and X-Ray Microanalysis* (Kluwer Academic/Plenum, 2003).
52. H. J. Leamy, "Charge collection scanning electron-microscopy," J. Appl. Phys. **53**, R51–R80 (1982).
53. D. Rugar and P. Hansma, "Atomic force microscopy," Phys. Today **43**(10), 23–30 (1990).
54. R. Zhou, C. Edwards, A. Arbabi, G. Popescu, and L. L. Goddard, "Detecting 20 nm wide defects in large area nanopatterns using optical interferometric microscopy," Nano Lett. **13**, 3716–3721 (2013).
55. Y. Park, G. Popescu, K. Badizadegan, R. R. Dasari, and M. S. Feld, "Fresnel particle tracing in three dimensions using diffraction phase microscopy," Opt. Lett. **32**, 811–813 (2007).
56. R. Zhou, C. Edwards, G. Popescu, and L. L. Goddard, "9 nm node wafer defect inspection using visible light," Proc. SPIE **9050**, 905017 (2014).